PERGAMON

International Journal of Heat and Mass Transfer 44 (2001) 1053–1063

International Journal of HEAT and MASS TRANSFER

www.elsevier.com/locate/ijhmt

Impingement cooling in triangular ducts using an array of side-entry wall jets

Jenn-Jiang Hwang [a,*], Chung-Shen Cheng [a]

[a] *Department of Mechanical Engineering, Chung-Hua University, Hsinchu 300, Taiwan, ROC*

Received 5 January 2000

Abstract

An experimental study has been performed to measure local heat transfer coefficients and static wall pressure drops in leading-edge triangular ducts cooled by wall/impinged jets. Coolant provided by an array of equally spaced wall jets is aimed at the leading-edge apex and exits from the radial outlet. Detailed heat transfer coefficients are measured for the two walls forming the apex using transient liquid crystal technique. Secondary-flow structures are visualized to realize the mechanism of heat transfer enhancement by wall/impinged jets. Three right triangular ducts of the same altitude and different apex angles of $\beta = 30°$ (Duct A), 45° (Duct B) and 60° (Duct C) are tested for various jet Reynolds numbers ($3000 \leqq Re_j \leqq 12\,600$) and jet spacing ($s/d = 3.0$ and 6.0). Results show that an increase in Re_j increases the heat transfer on both walls. Local heat transfer on both walls gradually decreases downstream due to the crossflow effect. At the same Re_j, Duct C has the highest wall-averaged heat transfer rate because of the highest jet center velocity as well as the smallest jet inclined angle. The distribution of static pressure drop based on the local through flow rate in the present triangular duct is similar to that of developing straight pipe flows. Average jet Nusselt numbers on the both walls have been correlated with jet Reynolds number for three different duct shapes.

1. Introduction

Performance of a gas turbine is strongly influenced by turbine inlet temperature as shown from the analysis of thermodynamics. To accommodate higher turbine inlet temperatures and still maintain the metal temperatures below acceptable limits, highly sophisticated cooling techniques are required, e.g., film cooling, jet-impingement, and augmented convection via roughness elements or pin fins. Owing to the external shape of blade, internal cooling cavities near the leading-edge often have a complex geometry, which can be simplified to a triangular channel for analytical or experimental analyses. Heat by conduction from the external pressure/suction surfaces is mostly convected away from the inner surfaces of the two principal walls forming the leading-edge apex to the internal coolant. Convective heat transfer is usually enhanced by using the ribs on the two or three walls of the triangular duct [1,2]. Also, jets impinging directly on the leading-edge apex [3] are an effective scheme to cool the blade leading-edge. This work involves the use of a combination of the wall jet cooling and the impinged-jet cooling to the blade leading-edge circuit. As shown in Fig. 1, side-entry jets injecting tangentially into the leading-edge triangular duct traverse one principal wall, then directly impinge on the apex as well as another principal wall, and finally exit radially from the blade tip. In this circumstance, either wall jets or impinged jets enhance the heat transfer on two principal walls of the triangular duct and the apex itself.

In the past three decades, there has been a large amount of efforts to examine the heat transfer performance of impingement cooling as is found in blade cooling application. Gardon and Cobonpue [4] used a heat flux gage to determine local heat transfer coefficient between isothermal hot surface and jets of

* Corresponding author. Tel.: +886-35-374-281; fax: +886-35-373-771.

E-mail address: jjhwang@chu.edu.tw (J.-J. Hwang).

0017-9310/01/$ - see front matter
PII: S0017-9310(00)00141-1

Nomenclature

C_p pressure drop coefficient, $2\rho(P-P_0)/U^2$
C_p^* modified pressure drop coefficient, $2\rho(P-P_0)/U^{*2}$
c_p specific heat at constant pressure, kJ kg^{-1} K^{-1}
D_e equivalent hydraulic diameter of the triangular duct, m
d diameter of jet hole, Fig. 3, m
H height of the pressure chamber (also the divider), Fig. 3, m
h heat transfer coefficient, kJ m^{-2} K^{-1}
k thermal conductivity of the duct wall material, W m^{-1} K^{-1}
k_f air thermal conductivity, W m^{-1} K^{-1}
Nu local Nusselt number, $h\,D_e/k_f$
Nu_j local jet Nusselt number, $h\,d/k_f$
Nu_{js} span-average jet Nusselt number
$\overline{Nu}_j$ area-averaged jet Nusselt number of the target or bottom wall
$\overline{Nu}_s$ fully developed Nusselt number of a smooth pipe flow, $\overline{Nu}_s = 0.023Re^{0.8}\,Pr^{0.4}$
P wall static pressure, kPa
P_0 wall static pressure at the first taps, kPa
Q_j volume flow rate across the jet hole, m^3 s^{-1}
Re Reynolds number based on D_e and U, i.e., UD_e/v
Re_j jet Reynolds number, $u\,d/v$
s jet spacing, Fig. 3, m
T_m mainstream temperature, K
T_i initial wall temperature, K
T_w wall temperature, K
t transient test time, s
U through flow velocity at the exit of the triangular duct, m s^{-1}
U^* local through flow velocity, m s^{-1}
u jet velocity, m s^{-1}
W_b width of the bottom plate, Fig. 3, m
W_t width of the target plate, Fig. 3, m
x coordinate paralleled with the bottom wall, Fig. 3, m
y coordinate normal to the bottom wall, Fig. 3, m
z streamwise coordinate, Fig. 3, m

Greek symbols

α thermal diffusivity of the duct wall material, s^{-1} m^2
α' angle between jet direction and duct axis
β apex angle opposite the divider, Fig. 3
β' jet inclined angle with respect to the target wall, i.e., $\beta' = 90^\circ - \beta$
ρ air density, kg m^{-3}
v viscosity of the air, s^{-1} m^2

Subscripts

b bottom wall
i initial
j jet
m mainstream
s smooth
t target wall
w wall

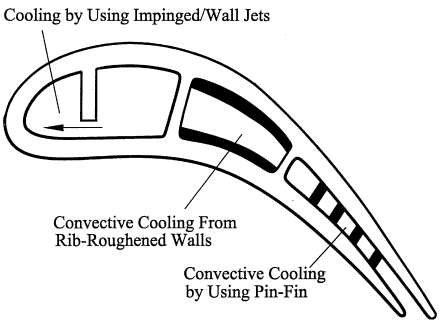

Fig. 1. Conceptual view of the wall/impinged jet cooling in the leading-edge circuit.

cooling air. Then, Gardon and Akfirat [5] dealt with the particular role of turbulence in the heat transfer of impinging jets, and the effects of jet Reynolds number, jet size, and jet travel distance were detected. Chupp et al. [6] evaluated the internal heat transfer coefficient for impingement cooling on the leading-edge of a turbine blade, and correlation for impingement heat transfer were developed in the presence of crossflow. Kercher and Tabakoff [7] measured the average flat-plate heat transfer coefficients for multiple, square array, round impinging air jets from a perforated plate. Their study included measurements of 16 different combinations of hole spacing and channel height, and correlations of heat transfer performance in the semi-enclosed environment were presented in terms of individual spanwise row jet and crossflow velocity. Florschuetz et al. [8–10] carried out a series of experiments to determine heat transfer characteristics for jet array impingement under different crossflow conditions. They presented correlations for both in-line and staggered holes patterns, including the effects of jet spacing, jet travel distance, and jet Reynolds number. Metzger and Bunker [11], and Bunker and Metzger [3], respectively, studied impingement cooling on turbine airfoil leading-edge apex with and without coolant extraction. The effects of jet Reynolds number, leading-edge sharpness, jet spacing, and jet travel distance were

examined. Results showed that the heat transfer rate was primarily dependent on the 0.6 power of jet Reynolds number and influenced slightly from the coolant extraction rate. In addition, the heat transfer rate increased with decreasing leading-edge sharpness and decreasing jet travel distance. Van Treuren et al. [12] measured the detailed heat transfer coefficients as well as the adiabatic wall temperatures under impinging jets by using the liquid crystal method. They used the hue saturation intensity (HIS) methods for analyzing the liquid crystal color changes. Huber and Viskanta [13,14] studied the effect of jet spacing and compared heat transfer from target plate perimeter and center jet-impingement in a confined, impinged array of axisymmetric air jets, but the crossflow effect was not considered. Recently, swirl fluid flow and heat transfer characteristics in a circular channel with lengthwise continuous tangential jets were examined in detail by Ligrani et al. [15], Hedlund et al. [16], and Moon et al. [17]. Ligrani et al. [16] performed a flow visualization study to examine the relation between the generation of Görtlier vortices and the augmented heat transfer characteristics in the cooling passage. Additional details of the pressure distribution and heat transfer measurements in the swirl chamber closely simulating the flow and wall-to-coolant temperature ratio in the swirl-cooled blade are presented in a parallel study by Hedlund et al. [16]. Huang et al. [18] measured the detailed heat transfer coefficient on the target wall with an array of orthogonal impinging jets by using transient liquid crystal technique. The effects of jet Reynolds number and exit flow orientation were examined. It was found that the flow exiting from both sides of the duct performed the best heat transfer on the target surface. Hwang and Cheng [19] also used the transient liquid crystal technique to investigate the swirl cooling characteristics in a triangular duct with an array of the inclined jets impinging on the triangle apex. The angle between the inclined jets and the duct axis varied from $\alpha' = 30°$ to 75°.

The objective of the present study is to extend the authors' previous work [19] to examine the effects of duct shape and jet spacing on the heat transfer and pressure drop characteristics in triangular ducts. The tangential jets from the side-entry are perpendicular to the duct axis, i.e., $\alpha' = 90°$, and directly impinge on the apex of the triangular duct. In the present study, detailed heat transfer coefficients on two principal walls of the triangular duct are measured by using transient liquid crystal technique. In addition, smoke-injection flow visualization and static pressure drops across the triangular duct with wall/impinged jets are measured. The present results in conjunction with those in the previous work may improve the understanding of the multiple wall/impinged jets cooling technique, providing the next step toward the application for the high-effective internal cooling methods for the leading-edges of turbine blades.

2. Experimental program

2.1. Experimental apparatus

Fig. 2 shows the entire apparatus employed in the present work, including a flow circuit, test section, and instruments. Compressed air from a blower passes through a flow meter that measures the volume flow rate of the airflow, and then flows into an electric heater to be heated to a required temperature. The hot air from the heater subsequently traverses a settling chamber for reducing the possible noise, a pressure chamber, then injects into the test section from the side-entry, and finally exits from the straight outlet of the triangular duct. Fig. 3 shows the detailed configuration, dimension and coordinate system of the test section. The entire triangular test section associated with the pressure chamber is made of Plexiglas® plates. Fifteen holes drilled through the low end of the divider between the pressure chamber and the triangular duct are tangent to the duct inner surface. The angle between the jet flow and the duct axial direction is 90°. With respect to these jets, the two walls that forms the apex β are referred to the "target wall" and the "bottom wall", respectively; while the remainder wall facing the apex is called the "divider". In general, conductive heat from the blade external pressure and suction surfaces is mostly removed convectively from the surfaces of the bottom and target walls; therefore only these two walls are coated with liquid crystals for heat transfer measurement. Three different shapes of triangular ducts shown in Fig. 4 are tested in the present work, i.e., 30°–90°–60° (Duct A), 45°–90°–45° (Duct B), and 60°–90°–30° (Duct C). The altitude of each triangular duct (i.e., height of the divider) is fixed at 30 mm, and the other flow and geometric parameters for each duct are also shown in Fig. 4.

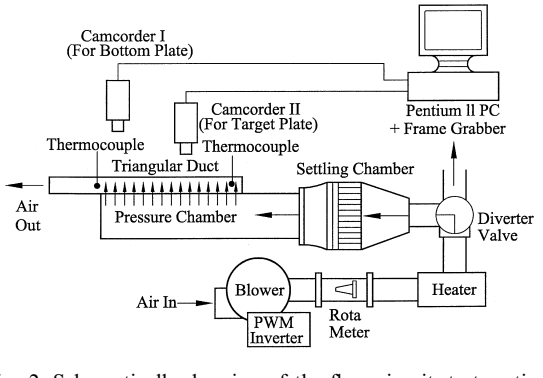

Fig. 2. Schematically drawing of the flow circuit, test section, and the instrumentation.

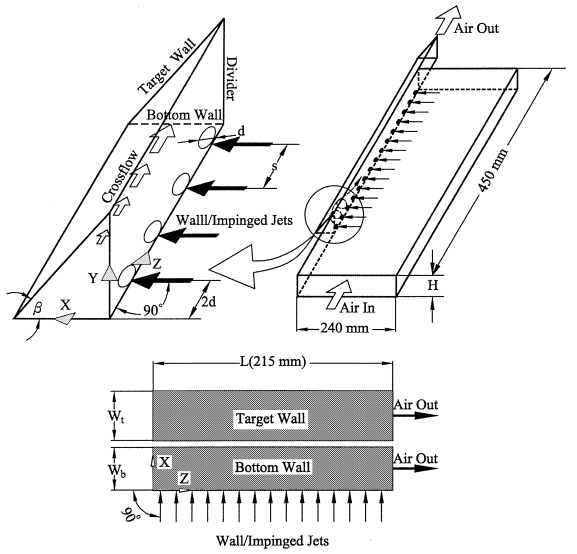

Fig. 3. Dimension and coordinate system of the wall/impinged jet cooling test section.

As shown in Fig. 2, two thermocouples located at the duct inlet and outlet, respectively, are connected to a real-time analyzing recorder (YOKOGAWA, AR 1100A) to measure the mainstream temperature history. The bottom and target walls are respectively installed 13 pressure taps for the static-pressure measurement. They are connected to a micro-differential transducer and a conditioner to amplify the pressure signals, which are subsequently transferred to a digital readout.

The time of color change of the liquid crystals during a transient test is measured by using two digital color camcorders (SONY DCR-TRV7) and a computer vision system (including a frame grabber interface associated with a Pentium II personal computer). The two camcorders are focused on the liquid-crystal-coated bottom and target walls to view and record their color changes

Duct	A	B	C
β	30°	45°	60°
De (mm)	22.0	17.6	12.7
d (mm)		5.0	
s (mm)		15.0, 30.0	
Re_j (u d/ν)		3000 - 12600	
Re (UDe/ν)		8600 - 21000	

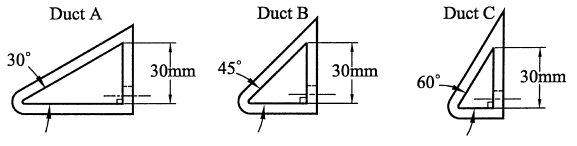

Fig. 4. Shapes of the triangular duct investigated and the associate parametric variations.

during the transient test. A frame grabber interface is programmed to analyze the color changes using image-processing software. The software analyzes the picture frame-by-frame and simultaneously records the time lapse of the liquid crystals from colorless to green during the transient test.

2.2. Theoretical basis

The local heat transfer coefficient over the test surface can be obtained by assuming one-dimensional transient conduction over a semi-infinite solid with the solution [20]

$$\frac{T_w - T_i}{T_m - T_i} = 1 - \exp\left(\frac{h^2\alpha t}{k^2}\right)\mathrm{erfc}\left(\frac{h\sqrt{\alpha t}}{k}\right). \quad (1)$$

By knowing the wall temperature (T_w) the initial surface temperature (T_i), the oncoming mainstream temperature (T_m), and the corresponding time (t) required to change the coated-surface color to green at any location, the heat transfer coefficient h can be calculated from Eq. (1) the above equation. In a typical run, the time required for the color changes is about 15–90 s depending on the location, mainstream temperature, and through flow rate. This testing time is so short that the heat flow can hardly penetrate the depth of Plexiglas®. Therefore, the assumption of the semi-infinite solid on the test surface is valid. Since T_m is time-dependent, the solution in Eq. (1) should be modified. First, the mainstream temperature history is simulated as a series of time step changes. Then, the time step changes of the mainstream temperature are included in the solution for the heat transfer coefficient using Duhamel's superposition theorem. The solution for the heat transfer coefficient at every location is therefore represented as eject

$$T_w - T_i = \sum_{j=1}^{n}\left\{1 - \exp\left[\frac{h^2\alpha(t-\tau_j)}{k^2}\right] \times \mathrm{erfc}\left[\frac{h\sqrt{\alpha(t-\tau_j)}}{k}\right]\right\}\left[\Delta T_{m(j,j-1)}\right], \quad (2)$$

where $\Delta T_{m(j,j-1)}$ and τ_j are the temperature and time step changes obtained from the recorder output, the maximum uncertainty of h is an order of ±6.8%. The individual contributions to the uncertainty of h for the measured or physical properties are: time of the color change t, ±2.8%, mainstream temperature T_m, ±3.0%, and wall material properties α and k, ±3.0%.

Transient test of the heat transfer measurement was thus carried out by the following procedures. First, the bottom and target surfaces are sprayed with liquid crystals and then black paints. Then, the test section is assembled, and each interface is sealed with petroleum for preventing the air leakage. The camcorders are set up and focused on these surfaces. Each test run is thermal

transient, initiated by suddenly exposing the hot air to the test section, which results in a color change of the surface coatings. Before the test run, the hot air bypasses the test section so that the walls remain at the laboratory ambient temperature. The valve is kept in the diverted position until a required mainstream temperature has been achieved in the diversion flow loop. Then, the valve turns to route the hot air into the test section and, simultaneously, the recorder is switched on to record the main-stream temperature history. The image processing system records the transition time for the color change to green, and transfers the data into a matrix of time of the color change over the entire surface. The time and temperature data are entered into a computer program to obtain the local heat transfer coefficient.

2.3. Data analysis and uncertainty

The nondimensional heat transfer coefficient on the target and bottom walls of the triangular duct with wall/impinged jets is represented by the jet Nusselt number as

$$Nu_j = hd/k_f. \tag{3}$$

The static pressure distributions along the triangular duct, either on the bottom wall or on the target wall, can be made dimensionlessly as

$$C_p = 2(P - P_0)/(\rho U^2), \tag{4}$$

where P_0 is the reference wall static pressure at the first pressure tap and U is the average velocity at the duct exit. The pressure-drop coefficient obtained is based on adiabatic conditions (i.e., test with ambient-temperature mainstream). By using the estimation method of Kline and McClintock [21], the maximum uncertainties of the investigated nondimensional parameters are 8.5% for Nu_j, and 7.7% for C_p.

3. Results and discussion

Before the subsequent discussion of heat transfer in triangular ducts with wall/impinged jets, it is important to verify the present experimental data by comparing with previous results. Fig. 5 shows the distributions of dimensionless local heat transfer coefficient, Nu, on the bottom wall of Duct A with straight flow. Airflow direction is from left to right. It is introduced from an upstream plenum and enters the triangular duct through a sharp-edge entrance. Transient liquid crystal measurements are undertaken in the region between $2.0 \leqq z/D_e \leqq 23.0$. It is seen from this figure that the entrance effect significantly decreases the heat transfer along the axial distance. Since the sidewall effect caused by the target wall (β corner) reduces the heat transfer rate more significantly than that by the divider (right-angle corner), the heat transfer near the target wall is lower than that near the divider at the same axial station. Thus, the tongue-shaped Nusselt number distributions are deflected toward to the divider. Table 1 shows the comparison of developing heat transfer between the present triangular-duct results and the previous results in a circular pipe with a 90° sharp-edged entrance [22]. Since in the triangular duct the heat transfer coefficients vary around the periphery, the present heat transfer coefficient at each axial location is averaged not only over the span distance (X) of the entire bottom wall but also over an axial distance (Z) of

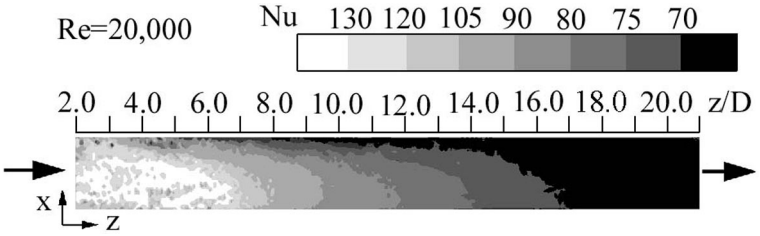

Fig. 5. Developing heat transfer on the bottom wall of the triangular duct with sharp-edged entrance and straight flow between $2.0 \leqq z/D_e \leqq 23.0$.

Table 1
Comparison of developing heat transfer between the present and previous works

Duct distance, z/D_e		2.0	4.0	6.0	8.0	10.0	20.0
Present work ($Re = 20\,000$)	Nu	127.4	120.3	97.9	91.0	78.8	68.9
	$Nu/\overline{Nu}_s$	2.23	2.11	1.70	1.58	1.36	1.19
Mills (1962) [22]		2.36	1.95	1.73	1.60	1.54	1.28
Deviation		5.5%	8.2%	1.7%	1.38%	10.3%	6.3%

$\pm 0.2D_e$ to fairly compare with the constant circumferential data of a circular pipe [22]. As shown in this table, the agreement between the present results and the previous results is satisfactory, with the maximum deviation less than 11%. This comparison has implied that the present experimental procedure is adequate and the present data are reliable.

3.1. Flow distributions

Flow rate through each jet hole is highly related to the local heat transfer characteristics in the triangular duct. Therefore, the static pressure differences between the pressure chamber and the triangular test section are measured to determine each jet flow rate. The local pressure distributions are measured by placing the static pressure taps inside the test section and the pressure chamber. Static pressures are measured at each jet location for each jet Reynolds number. The axial distributions of the static pressure difference across each jet hole is shown in Fig. 6(a) for various jet Reynolds numbers, while the corresponding distributions of the flow rate through each jet hole and the crossflow rate is displayed in Fig. 6(b). It is seen that the higher the jet velocity the larger is the pressure drop across each jet holes. Moreover, the static pressure drop across each jet hole (also the jet flow rate) increases with the axial location. This is because not only the static pressure in the pressure chamber increases downstream since the air comes to a stop at the end for pressure chamber, but also the static pressure in the triangular duct decreases as z/d increases. Florschuetz et al. [9] and Parsons et al. [23] found similar trends. As shown in Fig. 6(b), the flow rate through each jet hole increases slightly with an increase in the channel distance, while the crossflow increases linearly almost with an increase in the channel distance.

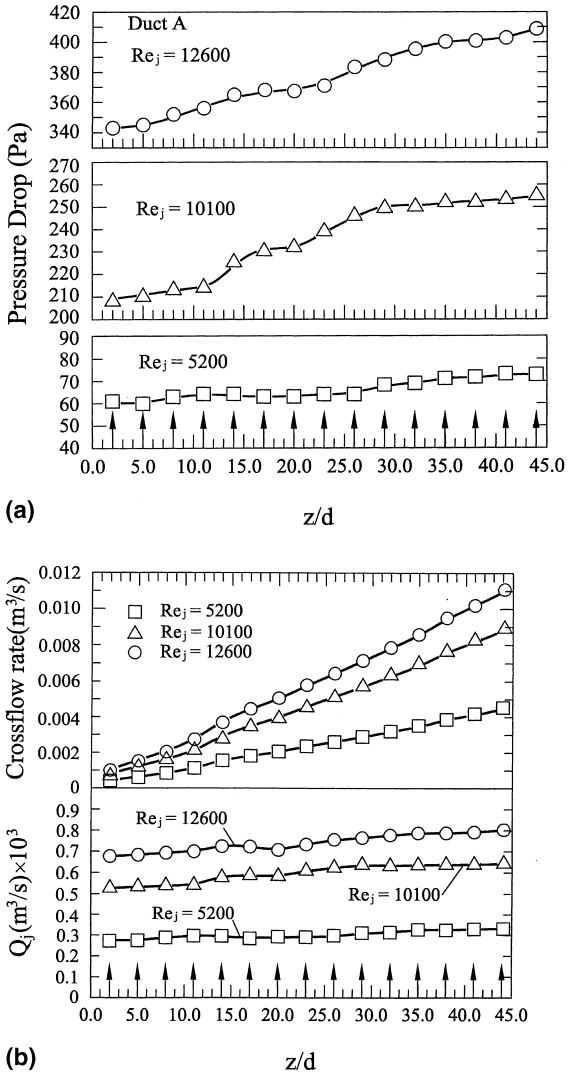

Fig. 6. (a) Static pressure drop across each jet hole for different jet Reynolds number; (b) jet flow rate and the crossflow of as a function of z/d.

3.2. Heat transfer coefficient distribution

Fig. 7 shows the heat transfer coefficient distributions on the bottom (lower one) and target (upper one) walls for various jet Reynolds numbers, duct shapes, and jet spacings. The arrows shown typically on the Fig. 7(a) indicate the location and direction of the jets. The through flow exits from the right end of the graphs.

The effects of jet Reynolds number on the Nu_j distribution are given in Figs. 7(a)–(c) for the Duct A. The jet spacing is fixed at $s/d = 3.0$, and the jet Reynolds number varies from $Re_j = 5200$ to 12 600. Results show an increase in the jet Nusselt number for an increase in the jet Reynolds number. Near the upstream closed end for each jet Reynolds number, strong wall jets create high heat transfer bends across the bottom wall from the jet inlet to the apex β. Meanwhile, the wall jets impinge on the target wall at the corresponding axial locations that produce round zones of high heat transfer. The penetration depth of the wall jet on the bottom wall is gradually reduced as the flow develops in the Z direction, and simultaneously the jet direction has been slightly deflected toward streamwise direction. On the target wall, high heat transfer zones are also gradually reduced and move to the span center of the target wall as the flow develops in the Z direction. The above facts are because of the effect of the swirl-motioned crossflow, which is increased downstream due to the flow accumulation (Fig. 6(b)). Note that the region of poor heat transfer on the target wall adjacent the corner opposed to the bottom wall is gradually reduced downstream, and however, the heat transfer near the region adjacent the apex β becomes poor downstream.

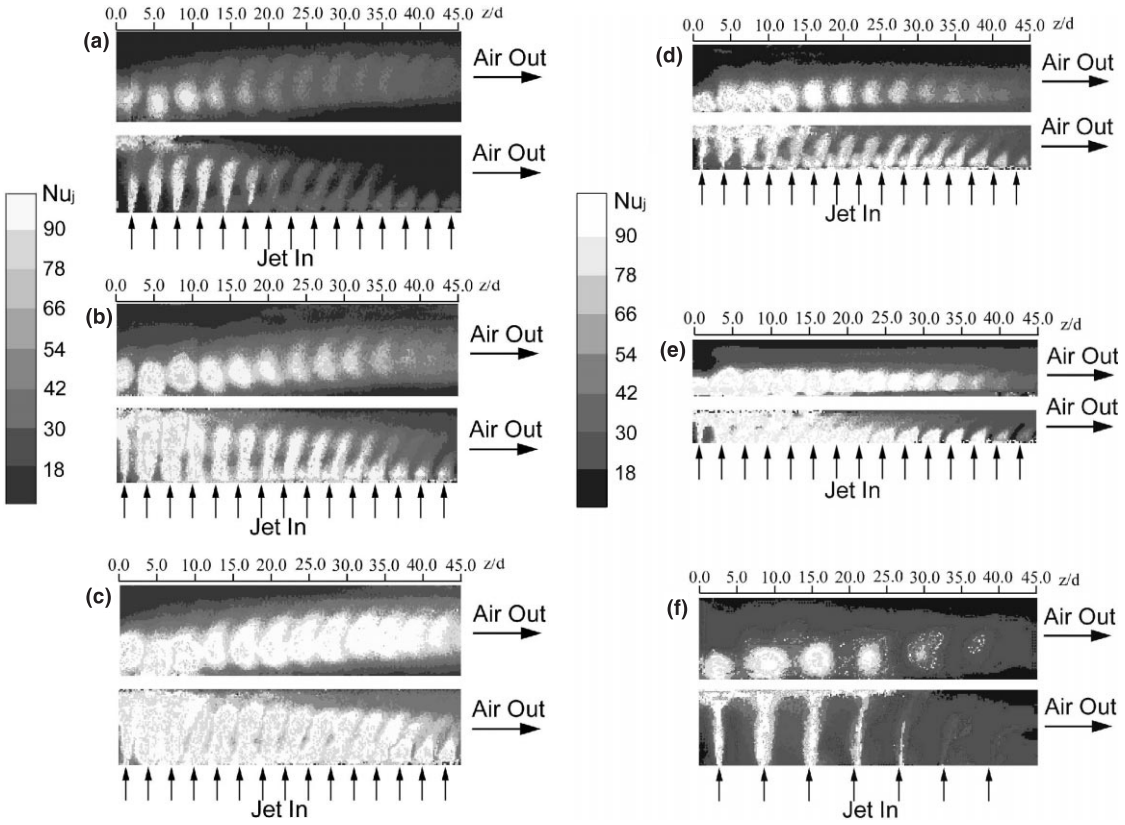

Fig. 7. Detailed heat transfer coefficient distribution on the bottom and target walls: (a) $Re_j = 5200$, $s/d = 3.0$, Duct A; (b) $Re_j = 10\,100$, $s/d = 3.0$, Duct A; (c) $Re_j = 12\,600$, $s/d = 3.0$, Duct A; (d) $Re_j = 5100$, $s/d = 3.0$, Duct B; (e) $Re_j = 5350$, $s/d = 3.0$, Duct C; (f) $Re_j = 10\,400$, $s/d = 6.0$, Duct A.

To confirm the heat transfer mechanisms above, the flow structures at different axial stations are visualized by using smoke-injection. Figs. 8(a)–(c) show the secondary-flow structures in Duct A at the axial planes cutting across the center of the second ($z/d = 5.0$), the fifth ($z/d = 17.0$), and the 11th ($z/d = 32.0$) jet holes from the upstream closed end, respectively. The jet Reynolds number for the three graphs is fixed at $Re_j = 5200$. The smoke from a smoke generator is injected into the pressure chamber as well as the test duct before the blower is turned on. A laser sheet constructed by passing a Helium–Neon laser beam (60 mW, Spectra Physics 120) through a rod of glass realizes the flow visualization [24]. A 35-mm single lens camera is focused on the illuminating plane. Photographs of the flow are taken on Agfa film with a shutter speed of 1/1000 s. It is seen from Fig. 8(a) that the jet from the second hole traverses thoroughly the bottom wall and then directly impinges on the apex β. Dense smoke keeping in the corner opposed to the bottom wall means that the flow is relatively stagnant in this region; hence a poor heat transfer (Fig. 7(a)). As for the photograph shown in Fig. 8(b), the jet exiting from the fifth hole turns into the mainstream before impinging on the apex, and thus creates a swirl-motioned secondary-flow close to the target wall. The swirl flow washes the target wall, and therefore creates a high heat transfer band spanning the target plate (Fig. 7(a)). At the 10th hole (Fig. 8(c)), the jet turns into the core flow after traversing only one-third of the bottom wall. Therefore, the wall jet phenomena on the bottom wall (Fig. 7(a)) become weak. Meanwhile, the jet flow can not reach and hence cool the apex, resulting in a dead zone near the apex β (Fig. 7(a)). Generally speaking, the comparison of the secondary-flow structures at different axial stations given in Fig. 8 has provided a good explanation of the detailed heat transfer coefficient distributions measured by liquid crystal technique.

The effect of duct shape on the distribution of detailed heat transfer coefficient is given by comparing Figs. 7(a), (d) and (e) under almost the same jet Reynolds number ($Re_j = 5200 \pm 3\%$). In these figures, the jet spacing is fixed at $s/d = 3.0$. It is seen from these three figures that, globally, Duct C has the highest heat transfer coefficients, and Duct B performs the better heat transfer than Duct A. Several reasons can explain

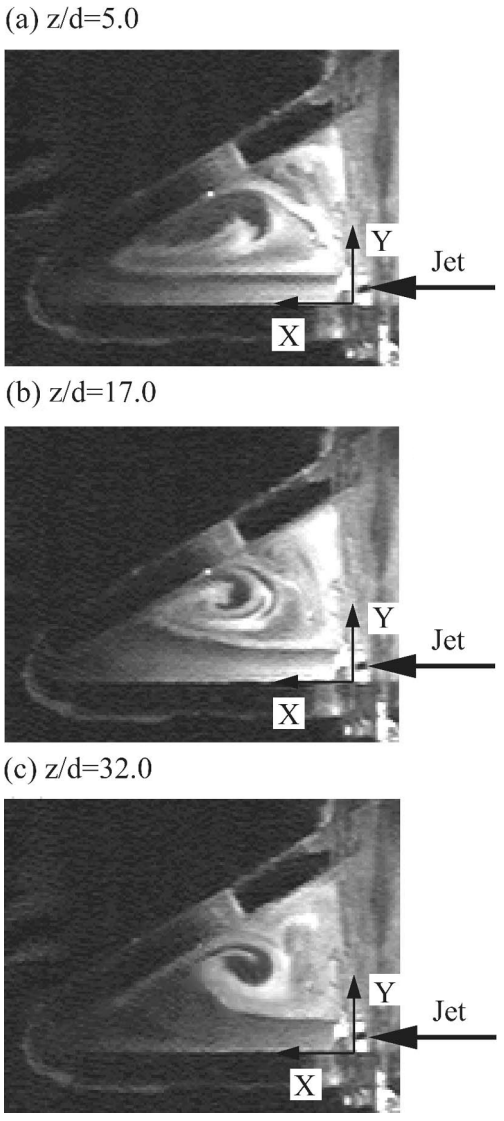

Fig. 8. Secondary flow structures visualized by smoke injection at several axial station of Duct A at $Re_j = 5200$: (a) $z/d = 5.0$; (b) $z/d = 17.0$; (c) $z/d = 32$.

this fact. First, of the same Re_j, the shorter the jet travel distance is, the higher the jet center (maximum) velocity is [25]. Then, the target wall for Duct C has the smallest jet inclined angle (β'). Both these lead to the most significant traces of heat transfer enhancement on the target wall (jet-impingement) and the bottom wall (wall jet) for the Duct C. The last reason is that Duct C has the strongest force advection by primary and secondary-flows of the highest duct through velocity. Note that because the jets for the Ducts B and C can penetrate the bottom-wall width almost for the entire duct length, the dead zone near the apex β becomes insignificant.

Comparing Fig. 7(a) with Fig. 7(f) illustrates the effect of jet spacing on the detailed heat transfer distributions for Duct A under the same duct through flow rate. Because the jet velocity for $s/d = 6.0$ is double as compared to that for $s/d = 3.0$, the wall jet as well as jet-impingement phenomena become more significant for Fig. 7(f) than that for Fig. 7(a). However, the heat transfer distribution is so localized that it can not promote the overall heat transfer performance too much on both the bottom and target walls.

3.3. Span-averaged Nusselt number distribution

The effects of Reynolds number on the span-averaged jet Nusselt number distributions along the axial distance of the Duct A are shown in Fig. 9. The upper and lower graphs represent the results of the target and bottom walls, respectively. An array of arrows on each graph indicates the location and direction of the jets. The span-averaged jet Nusselt numbers on the bottom and target walls of the duct decrease with increasing Re_j. In addition, the span-averaged jet Nusselt number has a repeated peak-valley distribution along the axial distance on both the bottom wall and the target wall. The local maximum of Nusselt number on the bottom and target walls, respectively, corresponds to the wall and impinged jets. Note that the axial locations of these local maximum values are slightly downstream with respect to the corresponding jet exits, especially for those on the target wall. This is again due to the crossflow effect.

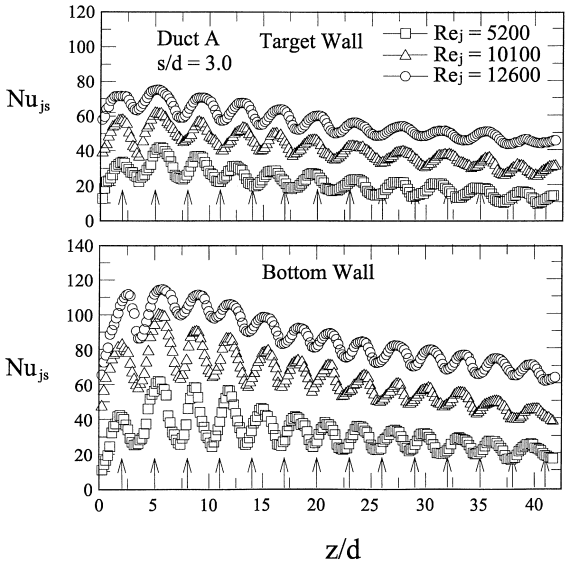

Fig. 9. Span-averaged jet Nusselt number along the axial distance.

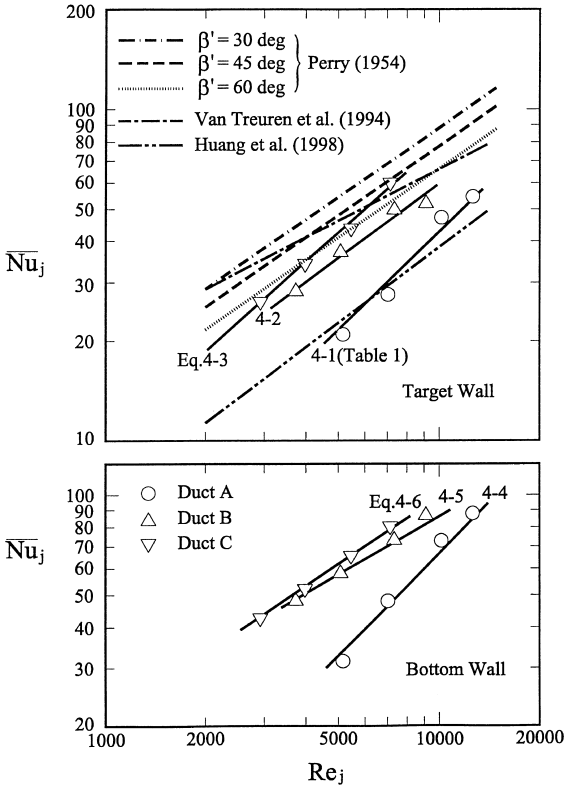

Fig. 10. Wall-averaged jet Nusselt number vs jet Reynolds number.

3.4. Wall-averaged Nusselt number

Fig. 10 shows the average jet Nusselt number ($\overline{Nu}_j$) on the bottom and target walls as a function of jet Reynolds number. The value of $\overline{Nu}_j$ is an average of the detailed results on the entire bottom or target wall. The present results for the three different duct shapes correlate for the jet Reynolds-number dependence as $\overline{Nu}_j = C_1 Re_j^{C_2}$ (solid lines). The coefficients of C_1 and C_2 for each duct shape and the deviations between the actual experiments and these correlations are displayed in Table 2. It is seen that the bottom wall has a higher area-averaged heat transfer than the target wall. In addition, the duct shape affects $\overline{Nu}_j$ significantly on the both walls. Under the same jet Reynolds number, the values of $\overline{Nu}_j$ on the target and bottom walls follow the same trend of the Duct C, the highest, and the Duct B greater than the Duct A. The reason has been described for the effects of duct shape on the local heat transfer distribution (Fig. 7). Note that the jet Reynolds-number dependence of $\overline{Nu}_j$ on the bottom wall for the Duct A is stronger than that for the other two ducts. This may be explained as follows. At low Re_j, a large portion of the duct walls for the Duct A is not sensitive to the wall/impinged jets (Fig. 7(a)). An increase in Re_j will enhance the wall jets that spread a larger portion of the bottom wall, and thus promote significantly the area-averaged heat transfer. Fig. 9 further shows the comparison of the present target-wall results of with the correlations by Perry [26], Van Treuren et al. [12] and Huang et al. [19] for the wall cooled by a single impinged jet or an array of impinged jets. In Perry's work, a single hot gas jet impinged on the target wall with different jet inclined angles of $\beta' = 30°, 45°$, and $60°$. Both the present and Perry's results revealed that the target wall heat transfer decreases with increasing the jet inclined angle. Quantitatively, the present data are smaller than Perry's data at the same jet inclined angle because of the lack of crossflow effect for the single jet in Perry's work. The correlation by Van Treuren et al. [12] was developed based on an array of 5 by 8 jets. The jet spacing in the spanwise and streamwise directions was fixed at $s/d = 8.0$. In Huang et al. [19], a total of 4 by 12 jet holes was distributed on the jet plate, and the jet spacing was $s/d = 4.0$. In both works, the jets impinge normally on the target wall (i.e., $\beta' = 0$). Qualitatively, all of the works reveal that the impingement heat transfer is increased with increasing jet Reynolds number, and is proportional to Re_j^m, where $0.5 < m < 1.0$. Quantitative comparison is not available because of much difference in the duct and jet geometry between the present work and those of Van Treuren et al. [12] and Huang et al. [19].

3.5. Static pressure drops

Fig. 11 shows the wall static pressure distribution along the axial distance of the target and bottom walls of the Duct C. The jet spacing is fixed at $s/d = 3.0$, and the jet Reynolds number varies from 3000 to 7200. On

Table 2
Coefficients of wall-averaged heat transfer correlations

Duct shape	$\overline{Nu}_j = C_1 Re_j^{C_2}$					
	Target wall			Bottom wall		
	C_1	C_2	Error	C_1	C_2	Error
Duct A	0.0051	0.9791	9.8%	0.0036	1.0661	5.4%
Duct B	0.0596	0.7501	8.5%	0.4214	0.5811	8.2%
Duct C	0.0204	0.9013	7.2%	0.1979	0.6764	2.9%

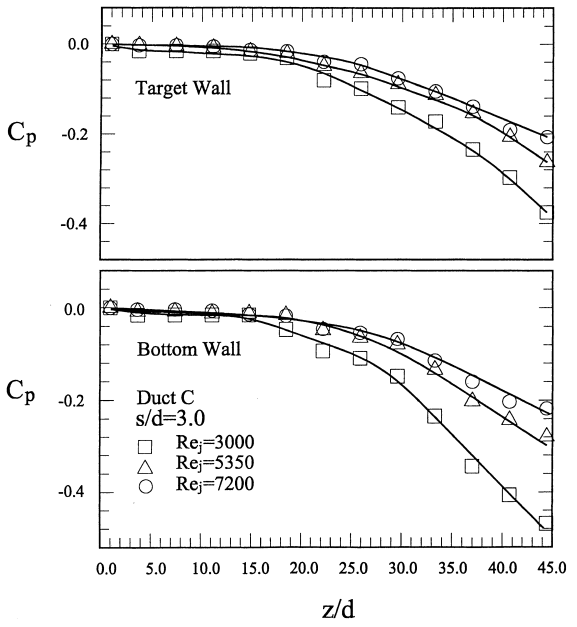

Fig. 11. C_p distributions along the axial distance of the triangular duct.

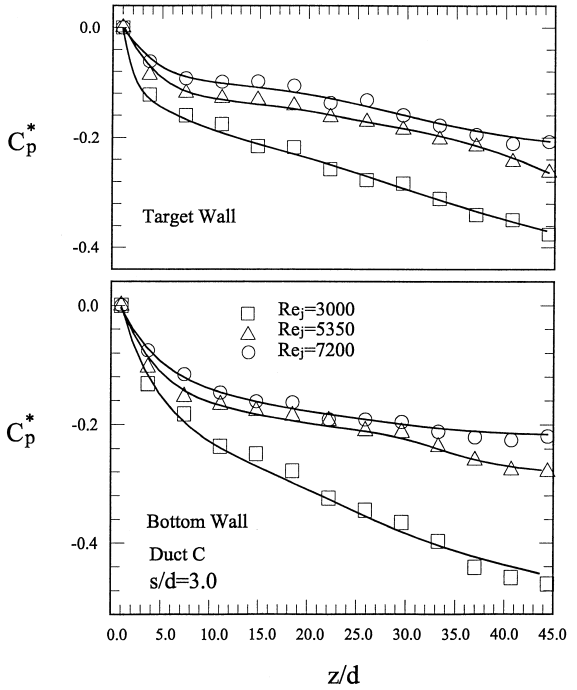

Fig. 12. C_p^* distributions along the axial distance of the triangular duct.

the both walls, the value of C_p drops more significantly for the low jet Reynolds number. It is further seen that the C_p on two principal walls has a similar distribution, i.e., it initiates a slight decrease from the upstream closed end and then drops sharply after about $z/d = 20$. This trend is different from that of a developing smooth pipe flow, in which the static pressure drops sharply at the entrance region and then decreases smoothly and in the fully developed region. This inconsistency is very reasonable because in the present duct with multiple side-entry jets the volume flow rate is accumulated downstream (Fig. 6(b)). Therefore, under the condition of the same through flow rate at the duct exit, the local nondimensional wall static pressure drop in the entrance region of the present duct is lowered down. Fig. 11 further shows the distribution of the modified static wall pressure drop based on the local volume flow rate. The modified pressure drop coefficient is defined as $C_p^* = 2(P - P_0)/(\rho U^{*2})$, where U^* is the local through flow velocity. It is seen from Fig. 12 that the trend of C_p^* distribution along the present swirl-flow channel is roughly similar to that of the developing straight pipe flow mentioned above.

4. Concluding remarks

Heat transfer and pressure drop characteristics in triangular ducts with multiple side-entry wall jets have been investigated experimentally in the present study. The effects of jet Reynolds number, duct shape and jet spacing are examined in detail. The heat transfer coefficient distributions on two principal walls of the triangular duct are measured using a transient liquid crystal technique so as to examine the effects of flow Reynolds number and jet inlet angle. Main findings based on the experiments are as follows.

(1) Local heat transfer coefficient distributions measured using transient liquid crystal technique in conjunction with the flow structures visualized via smoke-injection improved the understanding of the heat transfer enhancement in triangular ducts by wall/impinging jets encountering in the leading-edge cooling of the turbine blade. Also, they can be a reference for computational fluid dynamic-based studies relating to the wall/impinged-jet heat transfer.

(2) Heat transfer enhancement by wall/impinged jets on two principal walls is gradually decreased downstream due to the crossflow effect. On the bottom wall, not only the penetrability of the wall jet is reduced, but also, the jet has been deflected toward the downstream direction by the swirl-motioned crossflow. On the target wall, the swirl-motioned crossflow shifts the high heat transfer band from the apex to the span center of the target wall.

(3) Under the same jet Reynolds number, the Duct C has the highest area-averaged heat transfer on the two principal walls. This is because the Duct C has the strongest jet center velocity due to the shortest jet travel

distance together with smallest jet inclined angle with respect to the target wall, and the strongest forced advection due to the highest duct through flow velocity.

(4) Area-averaged Nusselt numbers on the bottom wall and the target wall have been correlated with Reynolds-number dependence for three different duct shapes.

(5) The C_p distribution along the present swirl-flow triangular duct with wall jets starts a slight decrease and then decreases sharply. When the pressure drop is normalized by the local duct through flow rate, it begins with a sharp decrease and then decreases slightly downstream. This trend is largely similar to that of the developing straight pipe flow.

Acknowledgements

The National Science Council of Taiwan under the contract number of NSC-88-2212-216-005 provides supports of this work.

References

[1] D.E. Metzger, R.P. Vedula, Heat transfer in triangular channels with angled roughness ribs on two walls, Exp. Heat Transfer 1 (1982) 31–44.
[2] Y.M. Zhang, W.Z. Gu, J.C. Han, Augmented heat transfer in triangular ducts with full and partial ribbed walls, AIAA J. Thermophys. Heat Transfer 8 (1994) 574–597.
[3] R.S. Bunker, D.E. Metzger, Local heat transfer in internally cooled turbine airfoil leading edge regions: part I – impingement cooling without film coolant extraction, Trans. ASME J. Turbomachinery 112 (1990) 451–458.
[4] R. Gardon, J. Cobonpue, Heat transfer between a flat plate and jets of air impinging on it, International Developments in Heat Transfer, in: Proceedings of the Second International Heat Transfer Conference, PART 2, ASME, New York, 454–460.
[5] R. Gardon, J.C. Akfirat, The role of turbulence in determining the heat-transfer characteristics of impinging jets, Int. J. Heat Mass Transfer 8 (1965) 1261–1272.
[6] R.E. Chupp, H.E. Helms, P.W. McFadden, T.R. Brown, Evaluation of internal heat-transfer coefficients for impingement-cooled turbine airfoils, J. Aircr 6 (1969) 203–208.
[7] D.M. Kercher, W. Tabakoff, Heat transfer by a square array of round air jets impinging perpendicular to a flat surface including the effect of spent air, Trans. ASME J. Eng. Power 92 (1970) 73–82.
[8] L.W. Florschuetz, R.A. Berry, D.E. Metzger, Periodic streamwise variations of heat transfer coefficients for inline and staggered arrays of circular jet with crossflow of spent air, Trans. ASME J. Heat Transfer 102 (1980) 132–137.
[9] L.W. Florschuetz, C.R. Truman, D.E. Metzger, Streamwise flow and heat transfer distributions for jet array impingement with crossflow, Trans. ASME J. Heat Transfer 103 (1981) 337–342.
[10] L.W. Florschuetz, D.E. Metzger, C.C. Su, Heat transfer characteristics for jet array impingement with initial crossflow, Trans. ASME J. Heat Transfer 106 (1984) 34–41.
[11] D.E. Metzger, R.S. Bunker, Local heat transfer in internally cooled turbine airfoil leading edge regions: part II – impingement cooling with film coolant extraction, Trans. ASME J. Turbomachinery 112 (1990) 459–466.
[12] K.W. Van Treuren, Z. Wang, P.T. Ireland, T.V. Jones, Detailed measurements of local heat transfer coefficient and adiabatic wall temperature beneath an array of impinging jets, Trans. ASME J. Turbomachinery 116 (1994) 369–374.
[13] A.M. Huber, R. Viskanta, Comparison of convective heat transfer to perimeter and center jet in a confined, impinging array of axisymmetric air jet, Int. J. Heat Mass Transfer 37 (1994) 3025–3030.
[14] A.M. Huber, R. Viskanta, Effect of jet–jet spacing on convective heat transfer to confined, impinging array of axisymmeteric air jet, Int. J. Heat Mass Transfer 37 (1994) 2859–2860.
[15] P.M. Ligrani, C.R. Hedlund, R. Thambu, B.T. Babinchak, H.-K. Moon, B. Glazer, Flow phenomena in swirl chambers, ASME Paper 97-GT-530, 1997.
[16] C.R. Hedlund, P.M. Ligrani, H.-K. Moon, B. Glazer, Heat transfer and flow phenomena in a swirl chamber simulating turbine internal cooling, ASME Paper 98-GT-466, 1998.
[17] H.-K. Moon, T. O'Connell, B. Glazer, Heat transfer enhancement in a circular channel using lengthwise continuous tangential injection, International Heat Transfer Congress, Seoul, South Korea, 1998.
[18] Y. Huang, S.V. Ekkad, J.C. Han, Detailed heat transfer distributions under an array of orthogonal impinging jets, AIAA J. Thermophys. Heat Transfer 12 (1998) 73–79.
[19] J.J. Hwang, T.S. Cheng, Augmented heat transfer in a triangular duct by using multiple swirling jets, Trans. ASME J. Heat Transfer 121 (1999) 683–690.
[20] J.P. Holman, Heat Transfer, 8th ed., McGraw-Hill, New York, 1997.
[21] S.J. Kline, F.A. McClintock, Describing uncertainties in single-sample experiments, Mech. Eng. 75 (1953) 3–8.
[22] A.F. Mills, Experimental investigation of turbulent heat transfer in the entrance region of a circular conduit, J. Mech. Eng. Sci. 4 (1962) 63–77.
[23] J.A. Parsons, J.C. Han, C.P. Lee, Rotation effect on jet impingement heat transfer in smooth rectangular channels with four heated walls and radially outward crossflow, Trans. ASME J. Heat Transfer 120 (1998) 79–85.
[24] J.J. Hwang, D.Y Lai, Three-dimensional laminar flow in a rotating multiple-pass square channel with sharp 180-deg turns, Trans. ASME J. Fluids Eng. 120 (1998) 488–495.
[25] H. Schlichting, Boundary Layer Theory, McGraw-Hill, New York, 1979.
[26] K.P. Perry, Heat transfer by convection from a hot gas jet to a plane surface, Proc. Ins. Mech. Eng. 68 (1954) 775–784.